Journal of Non-Newtonian Fluid Mechanics 247 (2017) 165–177

Contents lists available at ScienceDirect

Journal of Non-Newtonian Fluid Mechanics

journal homepage: www.elsevier.com/locate/jnnfm

The "avalanche effect" of an elasto-viscoplastic thixotropic material on an inclined plane

Cassio M. Oishi[a,*], Fernando P. Martins[a], Roney L. Thompson[b]

[a] Departamento de Matemática e Computação, Faculdade de Ciências e Tecnologia, Universidade Estadual Paulista "Júlio de Mesquita Filho", Presidente Prudente 19060-900, São Paulo, Brazil

[b] Department of Mechanical Engineering, COPPE, Universidade Federal do Rio de Janeiro, Centro de Tecnologia, Ilha do Fundão, Rio de Janeiro, Rio de Janeiro 21945-970, Brazil

ARTICLE INFO

Article history:
Received 30 March 2017
Revised 10 July 2017
Accepted 15 July 2017
Available online 19 July 2017

Keywords:
Elasto-viscoplastic thixotropic materials
Avalanche effect
Finite difference Marker and Cell method
Transient computations
Free-surface boundary conditions

ABSTRACT

The so-called *avalanche effect* is one of the fingerprints of thixotropic materials. This self-reinforcing process where the decrease in viscosity, due to a rejuvenation process triggered by a stress field, induces a motion which in turn contributes to decrease the viscosity again, is well exemplified by the inclined plane problem. In this situation, the material in its fully-structured state is placed on an inclined plane with respect to the gravity force which is responsible for the beginning of the breakdown process. These thixotropic systems generally have a yield stress, a strength that must be overcome in order to induce rejuvenation. In addition, they exhibit elastic features, especially in the pre-yield state. In the present work we numerically solve the transient evolution of an elasto-viscoplastic thixotropic material subjected to the action of gravity on an inclined plane. In order to handle with the moving free-surface boundary condition encountered in the *avalanche effect*, we have used a combination of the Marker-And-Cell (MAC) method with the front-tracking scheme. This formulation was successfully employed for this kind of material in the recent paper of Oishi et al. (2016) [28]. In the present work, we have adapted our finite difference formulation to analyze the effects associated with an extended Herschel–Bulkley model in the simulation of a transient complex free surface flow. Concerning the parameters of the flow curve, it is shown that the dimensionless yield stress (plastic number) is the most significant one. However, for a fixed plastic number, different combinations of dimensionless consistency index and dimensionless Newtonian viscosity plateau can lead to a diversity of responses. The thixotropic equilibrium time had a significant impact on shifting the instant when the flow regime changes from an accelerating (when the front part of the material accelerates) to a retardation one (when this front part decelerates). Higher elasticity, as captured by the Weissenberg number, led to longer distances covered by the material.

1. Introduction

Time-dependent materials can be found in many processes like the ones present in cosmetics, food, mining, and oil industries. They constitute a class of materials with an internal microstructure that presents a non-negligible delay between a change in the applied stress and the corresponding rearrangement of its microstructure. The material property that is usually associated with the structure state is viscosity. An important subclass of time-dependent materials is the thixotropic one [1–4]. In this case, the viscosity is a decreasing function of the applied stress and the changes in structure are reversible, i.e. when the stress is removed, structure builds up.

A major class of time-dependent systems are the viscoplastic ones, i.e. materials which possess a yield stress. This class of materials exhibit solid-like to liquid-like transition when the yield stress is overcome. Many yield-stress materials are thixotropic, and therefore the connections between viscoplasticity and changes in microstructure are important ones [5,6]. In addition, in the solid-like state, elasticity is significant in these materials while its importance decreases as structure decays. These observations have motivated the conception of models for elasto-viscoplastic thixotropic materials [2,7–13]. These models can be roughly divided into two groups. One that takes a viscoplastic model as a basis to which elasticity and thixotropic effects are added and another where a viscoelastic model is the starting point to which viscoplasticity and thixotropy are included. Discussions with respect to some advantages and disadvantages of these two types of elasto-viscoplastic

* Corresponding author.
E-mail address: cassiooishi@gmail.com (C.M. Oishi).

http://dx.doi.org/10.1016/j.jnnfm.2017.07.001
0377-0257/

models were conducted by Mewis and Wagner [3] and by Souza Mendes and Thompson [4].

Advances on the understanding of viscoplastic thixotropic materials have contributed to the investigation of geophysical flows like avalanches of snow, the flow of volcanic lava, the flow of mud and mining dejection. These flows are characterized by the action of gravitational forces on the process of rejuvenation and yielding of the material. The slump test (fifty-cent rheometer) [14–17] and the Bostwick consistometer device [18] are usual tools that are employed to measure the rheology of such complex materials. The dambreak is a controlled lab problem where the effects of the action of gravity can be investigated [19,20].

Due to the presence of gravity currents [21] associated with free-boundary conditions, it is crucial that these problems are tackled by a transient approach since the evolution of the material as its structure is being broken is an important part of the solution of the problem. In particular, the so-called *avalanche effect* constitutes one of the fingerprints of thixotropic phenomenon. As discussed by [22,23] the avalanche effect is the self-reinforcing process where the initial rejuvenation due to gravity (for example) that a fully-structured material experiences leads to a motion which in turn increases the applied stress and contributes to a new round of viscosity decrease.

In the present work we study the *avalanche effect* problem representing the material by an elasto-viscoplastic thixotropic model that was recently developed in a series of papers [11,24–27]. The transient numerical solution is provided through the finite difference scheme, as recently performed by Oishi et al. [28]. This numerical framework combines the MAC method with front-tracking for describing the free surface boundary condition in the presence of moving fluid interface. Moreover, the governing equations for mass and momentum are numerically solved via projection method (fractional step method) while the normal stress condition at free surface is treated by an implicit formulation. The latter strategy maintains good stability properties for dealing with low Reynolds number non-Newtonian free surface flows.

2. Mathematical formulation

The mathematical formulation is the same as the one presented in [28] and hence, we repeat here its dimensionless form for the purpose of being self-contained.

The flow curve that captures the relation between stress and shear rate is assumed to be associated with an apparent-yield-stress fluid that possesses a yield stress, τ_y, a power-law term, $K\dot{\gamma}^n$, and a constant viscosity term, $\eta_\infty\dot{\gamma}$.

Because of the nature of the problem, instead of adopting a characteristic velocity scale, U_c, we define a characteristic stress, τ_c, as a primitive quantity. Following [29], τ_c is defined as the maximum stress intensity, σ, of the domain, evaluated at $t = 0$. Therefore, τ_c, as well as the characteristic length scale, L_c, depends on the specific problem analyzed. In particular, the formal definition of τ_c for studying the *avalanche effect* in the present work is given by Eq. (37). No flow will happen if $\tau_c \leq \tau_y$, i.e. if the maximum stress intensity value does not overcome the yield stress. Accordingly, the characteristic velocity, U_c, is defined with respect to the maximum potential of destruction, the difference between the maximum stress at $t = 0$ and the yield stress. Needless to say, $U_c = 0$, in case $\tau_c \leq \tau_y$. From now on, we assume that τ_c exceeds τ_y. Because of the power-law term that confers a non-linear character with respect to a characteristic velocity, U_c is defined by the implicit equation

$$\tau_c = \tau_y + K\left(\frac{U_c}{L_c}\right)^n + \eta_\infty \frac{U_c}{L_c} \tag{1}$$

which can be made dimensionless using the characteristic stress, τ_c, as follows

$$1 = \tau_y^* + K^* + \eta_\infty^*, \tag{2}$$

where

$$\tau_y^* = \frac{\tau_y}{\tau_c}, \quad K^* = \frac{K}{\tau_c}\left(\frac{U_c}{L_c}\right)^n, \quad \eta_\infty^* = \frac{\eta_\infty}{\eta_c} \tag{3}$$

and $\eta_c \equiv \tau_c L_c/U_c$. In Eq. (1), K and n are the consistency and exponent of the power-law term in the flow curve.

We have used the following dimensionless variables:

$$\begin{aligned} t^* &= t\frac{U_c}{L_c}, \quad \nabla^* = L_c\nabla, \quad \mathbf{u}^* = \frac{\mathbf{u}}{U_c}, \\ \boldsymbol{\tau}^* &= \frac{\boldsymbol{\tau}}{\tau_c}, \quad p^* = \frac{p}{\rho U_c^2}, \quad \mathbf{g}^* = \frac{\mathbf{g}}{g}, \quad \mathbf{D}^* = \mathbf{D}\frac{L_c}{U_c}. \end{aligned} \tag{4}$$

Eq. (1) is based on the non-regularized version of the extended Herschel–Bulkley model considered here to represent the flow curve behavior.

The present work adopts a traditional approach to describe the structure level of the material, namely the use of a scalar quantity, $\lambda \in [0, 1]$, that is intended to capture the current structure state. The extreme values correspond to the minimum structured state ($\lambda = 0$) and the maximum structured state ($\lambda = 1$). We have adopted one of the simplest forms of evolution of the structure parameter, whose dimensionless form is found in Eq. (11), i.e. the rate of change of the structure level is an increasing function of the driving potential, the difference between the current and the equilibrium values of the structure parameter. The parameter that represents the importance of the thixotropic effects is the dimensionless equilibrium time, $t_{eq}^* = t_{eq}U_c/L_c$ which compares the thixotropic time with characteristic time of the flow.

Other dimensionless quantities used in this work are the ones associated with the connection between bulk quantities, like viscosity and elastic modulus, with the structure parameter. The dimensionless relaxation viscosity, $\eta^*(\lambda)$, is given by

$$\eta^*(\lambda) = \eta_0^{*\lambda}\eta_\infty^{*(1-\lambda)} - \eta_\infty^* \tag{5}$$

where the quantities η_0^* and η_∞^* are the fully structured and totally unstructured dimensionless values of viscosity, using η_c as a characteristic quantity. The elastic modulus, in turn, is connected with the structure parameter by the dimensionless function $f(\lambda)$, which is given by

$$f(\lambda) \equiv \frac{G}{G_0} = \exp\left[m\left(\frac{1}{\lambda} - 1\right)\right], \tag{6}$$

where m is a positive constant.

The dimensionless total stress, $\boldsymbol{\sigma}$, is given by

$$\boldsymbol{\sigma} = -p\mathbf{I}Re + 2\eta_\infty\mathbf{D} + \boldsymbol{\tau}^M, \tag{7}$$

where $\boldsymbol{\tau}^M$ is the non-Newtonian extra-stress tensor whose evolution equations is given by

$$\begin{aligned} &\frac{\partial\boldsymbol{\tau}^M}{\partial t} + \nabla\cdot(\mathbf{u}\boldsymbol{\tau}^M) - [(\nabla\mathbf{u})\cdot\boldsymbol{\tau}^M + \boldsymbol{\tau}^M\cdot(\nabla\mathbf{u})^{\mathrm{T}}] \\ &\quad = \frac{f(\lambda)}{Wi}\left[-\frac{1}{\eta(\lambda)}\boldsymbol{\tau}^M + 2\mathbf{D}\right]. \end{aligned} \tag{8}$$

Therefore, the versions of the mathematical modeling equations, omitting the asterisk symbol, are given by

$$\nabla\cdot\mathbf{u} = 0, \tag{9}$$

$$\frac{\partial\mathbf{u}}{\partial t} + \nabla\cdot(\mathbf{u}\mathbf{u}) = -\nabla p + \frac{1}{Re}\left(\eta_\infty\nabla^2\mathbf{u} + \nabla\cdot\boldsymbol{\tau}^M\right) + \frac{1}{Fr^2}\mathbf{g}, \tag{10}$$

$$\frac{\partial\lambda}{\partial t} + \nabla\cdot(\mathbf{u}\lambda) = \frac{1}{t_{eq}}\left(1 - \frac{\lambda}{\lambda_{eq}}\right). \tag{11}$$

This set of equations corresponds to i) Eq. (9), the continuity equation; ii) Eq. (10), the balance of momentum equation; iii) Eq. (8), the constitutive equation for the non-Newtonian stress, $\boldsymbol{\tau}^M$; iv) Eq. (11), the evolution equation for the structure parameter, λ. The dimensionless numbers corresponding to the Reynolds number, *Re*, the Froude number, *Fr*, and the Weissenberg number *Wi* are defined as

$$Re = \frac{\rho U_c^2}{\tau_c}, \quad Fr = \frac{U_c}{\sqrt{gL_c}}, \quad Wi = \frac{\tau_c}{G_0}, \tag{12}$$

where G_0 is the elastic modulus in the fully structured state. From now, all variables are presented without the asterisk symbol.

The thixotropic behavior of the material is taken into account in the mathematical modeling by the following strategy:

- Construct the deviatoric part of the non-dimensional stress, σ_{dev}, according to

$$\sigma_{dev} = \sqrt{\frac{1}{2}\,\mathrm{tr}\left[\left(\boldsymbol{\sigma} - \frac{1}{3}\mathrm{tr}(\boldsymbol{\sigma})\boldsymbol{I}\right)^2\right]}, \tag{13}$$

- Once obtained σ_{dev} and considering the flow curve of the form given by Eq. (1), solve the non-linear equation

$$\sigma_{dev} = \zeta(\dot{\gamma}_{eq})[\tau_y + K(\dot{\gamma}_{eq})^n] + \eta_\infty \dot{\gamma}_{eq}, \tag{14}$$

in order to calculate the non-dimensional equilibrium deformation rate value, $\dot{\gamma}_{eq}$. In Eq. (14), we have adopted

$$\zeta(\dot{\gamma}_{eq}) = \begin{cases} 1 & \text{if} \quad \tau \geq \tau_y \\ \dfrac{(\eta_0 - \eta_\infty)\dot{\gamma}_{eq}}{\tau_y + K(\dot{\gamma}_{eq})^n} & \text{if} \quad \tau < \tau_y \end{cases} \tag{15}$$

where

$$\tau = \sqrt{\frac{1}{2}\,\mathrm{tr}[\boldsymbol{\sigma}^2]}. \tag{16}$$

It is worth noticing that different functions could have been adopted in the place of the chosen one for $\zeta(\dot{\gamma}_{eq})$ as discussed by Oishi et al. [28]. This function transforms a model conceived to capture the behavior of a yield-stress material into a model for apparent-yield-stress fluids.

- Compute the equilibrium viscosity using the classical definition

$$\eta_{eq} = \frac{\sigma_{dev}}{\dot{\gamma}_{eq}}. \tag{17}$$

- Finally, determine $\lambda_{eq}(\sigma_{dev})$ corresponding to η_{eq} using the inverse of the viscosity function:

$$\lambda_{eq} = \frac{\ln \eta_{eq} - \ln \eta_\infty}{\ln \eta_0 - \ln \eta_\infty}, \tag{18}$$

i.e. using the inverse function of Eq. (5).

In the present paper, two types of boundary are used for studying the *avalanche effect*: rigid wall and free surface. For the rigid wall, we have enforced no-slip boundary conditions for the velocity field. On the free surface, the normal stress condition

$$\mathbf{n} \cdot \boldsymbol{\sigma} \cdot \mathbf{n}^T = 0, \tag{19}$$

and the tangential boundary condition

$$\mathbf{m} \cdot \boldsymbol{\sigma} \cdot \mathbf{n}^T = 0, \tag{20}$$

are imposed, where $\mathbf{n} = (n_x, n_y)$ denotes the outward unit normal vector to the boundary while $\mathbf{m} = (m_x, m_y)$ is the unit tangent vector.

Finally, the dynamic of the moving interface is modeled by the convection of virtual marker particles solving the following equation

$$\dot{\mathbf{x}} = \mathbf{u}, \tag{21}$$

where $\mathbf{u}$ is a known velocity field while $\mathbf{x}$ represents the position of the particles.

3. Overview of the numerical scheme and flow problem description

The finite difference numerical scheme employed to study the transient motions of an elasto-viscoplastic thixotropic material has been presented by Oishi et al. [28]. Thus, the solution procedure, assuming that at time $t = t_n$ the total tensor $\boldsymbol{\sigma}$, the structure parameter λ and the markers positions $\mathbf{x}$ are known, can be summarized using the following steps:

1. Solution of the thixotropy considering the structure parameter at an intermediate time-level $\overline{\lambda}^{(n+1)}$.
In the first step of the algorithm, the non-linear equation (14) is solved by a hybrid bisection and Newton–Raphson method. Once computed the equilibrium deformation rate, $\dot{\gamma}_{eq}$, by the solution of the non-linear equation, this value is used to obtain the equilibrium viscosity, η_{eq}, and the equilibrium structure parameter, λ_{eq}, using respectively Eqs. (17) and (18). This step of algorithm is completed solving Eq. (11) by a semi-implicit scheme:

$$\left(\frac{1}{\delta t} + \frac{1}{t_{eq}\lambda_{eq}}\right)\overline{\lambda}^{(n+1)} = \frac{\lambda^{(n)}}{\delta t} + \frac{1}{t_{eq}} - \nabla \cdot (\mathbf{u}^{(n)}\lambda^{(n)}), \tag{22}$$

where δt is the time-step.
2. Calculation of the non-Newtonian tensor at an intermediate time-level $(\overline{\boldsymbol{\tau}}^M)^{(n+1)}$.
The second step of the computational cycle is related to the solution of the constitutive equation (8) by the explicit forward Euler scheme, for instance:

$$\begin{aligned} \frac{(\overline{\boldsymbol{\tau}}^M)^{(n+1)} - (\boldsymbol{\tau}^M)^{(n)}}{\delta t} &= -\nabla \cdot (\mathbf{u}^{(n)}(\boldsymbol{\tau}^M)^{(n)}) \\ &+ [(\nabla \mathbf{u}^{(n)}) \cdot (\boldsymbol{\tau}^M)^{(n)} + (\boldsymbol{\tau}^M)^{(n)} \cdot (\nabla \mathbf{u}^{(n)})^{\mathbf{T}}] \\ &+ \frac{f(\overline{\lambda}^{(n+1)})}{Wi}\left[-\frac{1}{\eta(\overline{\lambda}^{(n+1)})}(\boldsymbol{\tau}^M)^{(n)} + 2\mathbf{D}^{(n)}\right]. \end{aligned} \tag{23}$$

It is worth remarking that the latest value of the structure parameter obtained in the first step, $\overline{\lambda}^{(n+1)}$, is imposed in Eqs. (5) and (6) for constructing, respectively, the relaxation viscosity, $\eta(\overline{\lambda}^{(n+1)})$, and the function $f(\overline{\lambda}^{(n+1)})$.
3. Computation of velocity and pressure fields.
In order to uncouple the velocity and pressure fields of the conservation equations (9) and (10), we have employed an adaptation of the projection method for viscoelastic free surface flows described in previous works [30,31]. Summarily, this step can be separated in the following sub-steps:
3.1. Based on the Crank–Nicolson/Adams–Bashforth discretization, the momentum equation (10) is solved for computing a provisional velocity field, $\tilde{\mathbf{u}}^{(n+1)} = (\tilde{u}^{(n+1)}, \tilde{v}^{(n+1)})$ with an approximated value of the pressure filed, denoted as $p^{(n)}$, i.e.,

$$\begin{aligned} \frac{\tilde{\mathbf{u}}^{(n+1)}}{\delta t} - \frac{\eta_\infty}{2Re}\nabla^2\tilde{\mathbf{u}}^{(n+1)} &= \frac{\mathbf{u}^{(n)}}{\delta t} + \frac{\eta_\infty}{2Re}\nabla^2\mathbf{u}^{(n)} - \frac{3}{2}\nabla \cdot (\mathbf{uu})^{(n)} \\ &+ \frac{1}{2}\nabla \cdot (\mathbf{uu})^{(n-1)} - \nabla p^{(n)} + \nabla \cdot (\boldsymbol{\tau}^M)^{(n+\frac{1}{2})} + \frac{1}{Fr^2}\mathbf{g}, \end{aligned} \tag{24}$$

where

$$\nabla \cdot (\boldsymbol{\tau}^M)^{(n+\frac{1}{2})} = \frac{1}{2}\left[\nabla \cdot (\boldsymbol{\tau}^M)^{(n)} + \nabla \cdot (\overline{\boldsymbol{\tau}}^M)^{(n+1)}\right]. \tag{25}$$

3.2. A correction of the pressure, named $\psi^{(n+1)}$, is obtained solving the Poisson equation

$$\nabla^2\psi^{(n+1)} = \nabla \cdot \tilde{\mathbf{u}}^{(n+1)}, \tag{26}$$

with homogeneous Neumann boundary condition imposed in the rigid wall. At the free surface, the following equation needs to be solved:

$$\frac{\psi^{(n+1)}}{\delta t} - \frac{2\eta_\infty}{Re}\left[\left(\frac{\partial^2\psi^{(n+1)}}{\partial y^2}\right)n_x^2 + \left(\frac{\partial^2\psi^{(n+1)}}{\partial x^2}\right)n_y^2 - 2\left(\frac{\partial^2\psi^{(n+1)}}{\partial x\partial y}\right)n_x n_y\right] - \frac{\eta_\infty}{2Re}\nabla^2\psi^{(n+1)} = \frac{2\eta_\infty}{Re}\left[-\left(\frac{\partial\tilde{v}^{(n+1)}}{\partial y}\right)n_x^2 - \left(\frac{\partial\tilde{u}^{(n+1)}}{\partial x}\right)n_y^2 + \left(\frac{\partial\tilde{u}^{(n+1)}}{\partial y} + \frac{\partial\tilde{v}^{(n+1)}}{\partial x}\right)n_x n_y\right] + \frac{1}{Re}\left[\left(\overline{\tau}_{xx}^M\right)^{(n+1)}n_x^2 + 2\left(\overline{\tau}_{xy}^M\right)^{(n+1)}n_x n_y + \left(\overline{\tau}_{yy}^M\right)^{(n+1)}n_y^2\right] - p^{(n)}, \tag{27}$$

where $(\overline{\tau}_{xx}^M)^{(n+1)}$, $(\overline{\tau}_{xy}^M)^{(n+1)}$ and $(\overline{\tau}_{yy}^M)^{(n+1)}$ are the components of the non-Newtonian tensor at an intermediate time-level.

3.3. The final velocity and pressure fields are updating, respectively, by the following equations:

$$\mathbf{u}^{(n+1)} = \tilde{\mathbf{u}}^{(n+1)} - \nabla\psi^{(n+1)}, \tag{28}$$

$$p^{(n+1)} = p^{(n)} + \frac{\psi^{(n+1)}}{\delta t} - \frac{\eta_\infty}{2Re}\nabla^2\psi^{(n+1)}. \tag{29}$$

More details about these sub-steps can be found in our recent paper [28].

4. Updating the structure parameter $\lambda^{(n+1)}$.
The step of the algorithm for computing $\lambda^{(n+1)}$ is basically a repetition of step 1 using the latest values of the variables, i.e.,

$$\left(\frac{1}{\delta t} + \frac{1}{t_{eq}\lambda_{eq}}\right)\lambda^{(n+1)} = \frac{\overline{\lambda}^{(n+1)}}{\delta t} + \frac{1}{t_{eq}} - \nabla\cdot\left(\mathbf{u}^{(n+1)}\overline{\lambda}^{(n+1)}\right). \tag{30}$$

5. Updating the non-Newtonian stress tensor $(\boldsymbol{\tau}^M)^{(n+1)}$.
The final non-Newtonian stress tensor is obtained solving Eq. (8) by the second order Runge–Kutta scheme, for instance:

$$\frac{(\boldsymbol{\tau}^M)^{(n+1)} - (\overline{\boldsymbol{\tau}}^M)^{(n+1)}}{\delta t} = \frac{1}{2}[\mathbf{F_1}(\mathbf{u}, \boldsymbol{\tau}^M, \lambda) + \mathbf{F_2}(\mathbf{u}, \boldsymbol{\tau}^M, \lambda)], \tag{31}$$

where

$$\mathbf{F_1}\left(\mathbf{u}, \boldsymbol{\tau}^M, \lambda\right) = \mathbf{F}\left(\mathbf{u}^{(n)}, (\boldsymbol{\tau}^M)^{(n)}, \overline{\lambda}^{(n+1)}\right) \tag{32}$$

and

$$\mathbf{F_2}\left(\mathbf{u}, \boldsymbol{\tau}^M, \lambda\right) = \mathbf{F}\left(\mathbf{u}^{(n+1)}, (\overline{\boldsymbol{\tau}}^M)^{(n+1)}, \lambda^{(n+1)}\right) \tag{33}$$

with

$$\mathbf{F}(\mathbf{u}, \boldsymbol{\tau}^M, \lambda) = -\nabla\cdot(\mathbf{u}\boldsymbol{\tau}^M) + [(\nabla\mathbf{u})\cdot\boldsymbol{\tau}^M + \boldsymbol{\tau}^M\cdot(\nabla\mathbf{u})^{\mathbf{T}}] + \frac{f(\lambda)}{Wi}\left[-\frac{1}{\eta(\lambda)}\boldsymbol{\tau}^M + 2\mathbf{D}\right]. \tag{34}$$

6. Treatment of the moving interface.
In the last step of the algorithm, the positions of the virtual markers are updated from time level $t = t_n$ to $t = t_{n+1}$. For this purpose, we use the second order Runge–Kutta scheme for solving Eq. (21) in order to obtain the final particle positions $\mathbf{x}^{(n+1)}$:

$$\frac{\overline{\mathbf{x}} - \mathbf{x}^{(n)}}{\delta t} = \mathbf{u}\left(\mathbf{x}^{(n)}, t_n\right), \tag{35}$$

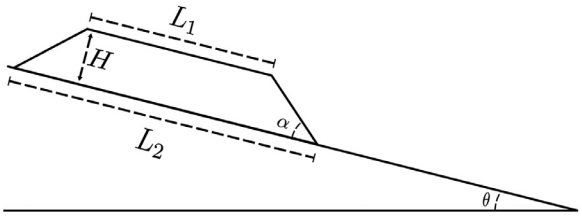

Fig. 1. Sketch view of the flow problem description.

$$\frac{\mathbf{x}^{(n+1)} - \mathbf{x}^{(n)}}{\delta t} = \frac{1}{2}\left[\mathbf{u}\left(\mathbf{x}^{(n)}, t_n\right) + \mathbf{u}(\overline{\mathbf{x}}, t_{n+1})\right], \tag{36}$$

where the velocities are calculated at the required positions using a bilinear interpolation from the nearest values in the mesh. The $\overline{\mathbf{x}}$ is an intermediate position (predictor) for the more accurate calculus using equation (36). More informations about this step can be found in previous works [30,31].

The flow problem addressed in this work is an isosceles trapezoid block of an elasto-viscoplastic material which is initially at rest in an inclined plane, as sketched in Fig. 1. The trapezoidal shape was chosen in order to avoid a possible tumbling that could happen in the case we chose the more natural rectangular shape. The top and bottom bases of the trapezoid block are considered with lengths $L_1 = 1$m and $L_2 = 5$m, respectively, while the angle of the bottom base is adopted as $\alpha = 45^\circ$. The height of trapezoid is used as a characteristic length of the problem, i.e., $L_c = H = 0.2$m. In $t = 0$, the front position, i.e., the most extreme right vertex of the trapezoid, is considered in the point (0, 0) of the Cartesian plan. The characteristic stress is given by

$$\tau_c = \frac{\rho g H}{\cos\theta}. \tag{37}$$

The influence of the slope is captured by varying the angle θ as will be shown in Section 4.

4. Results

4.1. Verification: a mesh refinement study

In order to present a verification of the method, we have simulated the transient evolution of an elasto-viscoplastic thixotropic material subjected to the action of gravity on an inclined plane considering three different meshes: M1 ($\delta x = \delta y = 0.05$), M2 ($\delta x = \delta y = 0.025$) and M3 ($\delta x = \delta y = 0.0125$). For this mesh refinement study, the following data were used: $\tau_y = 0.3$, $K = 0.5$, $t_{eq} = 100$, $\theta = 30^\circ$, $Fr = 0.0816$ and $Re = 0.01$.

The convergence of the free surface profile with the mesh refinement can be seen in Fig. 2. According to results described in this figure, one can see that the surface profiles of meshes M2 and M3 are near each other showing a good convergence with the mesh refinement. In particular, the resolution of the free surface around of the wall boundary on the right side of the block fluid for M2 and M3 is similar; thus in the remaining simulations, M2 mesh will be adopted.

4.2. Parametric studies on the dynamic of the "avalanche effect"

One important feature of the flow on the inclined plane is the progression of the front of the material as time elapses. In order to evaluate this evolution we compute the distance of the farther portion of the material with respect to the origin, $dist_x$, made dimensionless with the aid of the characteristic length, as presented in Fig. 2.

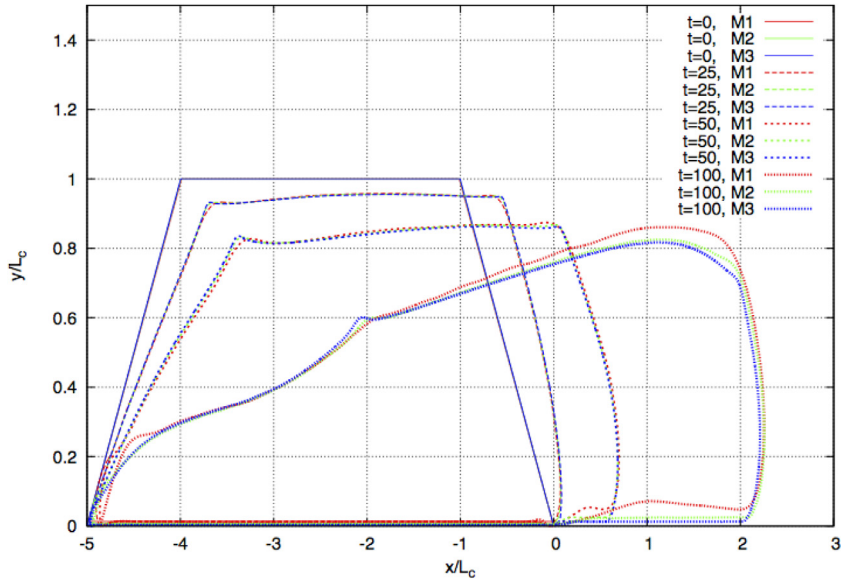

Fig. 2. Free surface profiles at selected times ($t = 0$, $t = 25$, $t = 50$ and $t = 100$) on meshes M1, M2 and M3 using $\theta = 30^{\circ}$.

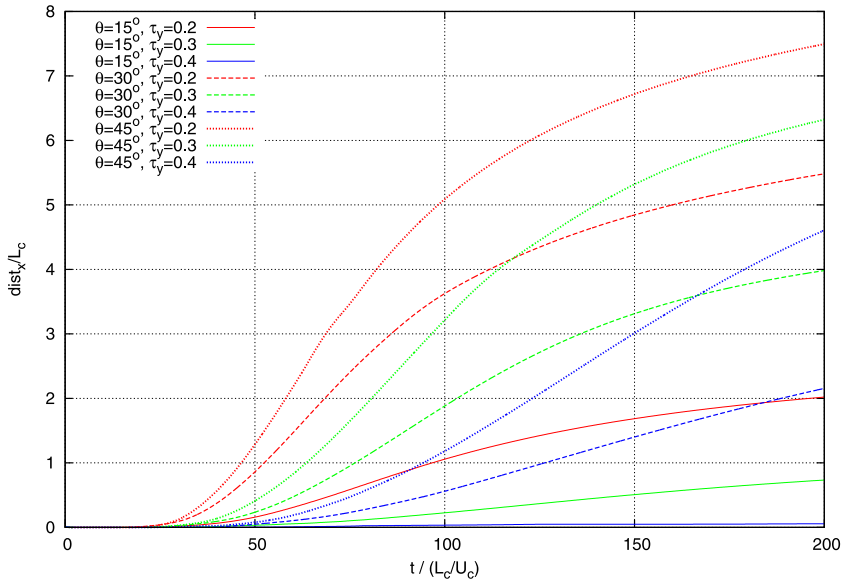

Fig. 3. Time variation of the front position, $dist_x$, varying the inclination angle and the plastic number. (For interpretation of the references to color in the text, the reader is referred to the web version of this article.)

Fig. 3 shows a number of this kind of evolution with respect to the dimensionless time, tU_c/L_c. These first results compare inclination angles of 15°, 30°, and 45° and plastic number of 0.2, 0.3, and 0.4, for fixed values of $Wi = 0.1$, $K = 0.5$, and $t_{eq} = 100$. Fixing the inclination, represented by a particular type of line, we can find the expected result that, once the plastic number is increased, the different colors show that, the front velocity is slower and the front portion of the material takes a longer dimensionless time to evolve. In general, this evolution shows two regimes: an accelerating regime followed by a retardation one. We can observe that lower values of plastic number induces earlier inflection points. However, in some cases, time ends before the achievement of the inflection point. For the highest value of plastic number and the lowest inclination angle (blue full line), the material almost does not move.

The corresponding evolution in time of the shape as well as the field of the structure parameter associated with the cases analyzed in Fig. 3 are shown in Figs. 4–7 where each figure is associated with a specific dimensionless time, from $tU_c/L_c = 25$ to $tU_c/L_c = 200$. In every case, a fully structured state is set as initial condition. It is interesting to notice that, during a first elapsed time, the trapezoidal shape does not change, while the structure parameter is evolving towards less structured states. This fact is a fingerprint of having the stress as the breaking agent, since the material experiences a significant rejuvenation process even with a vanishing deformation rate. At this stage, this evolution is mainly due to the action of gravity. For example, at $tU_c/L_c = 25$, Fig. 4, for the pair ($\theta = 45^{\circ}$, $\tau_y = 0.4$), we can notice that breaking is happening near the solid surface, but not near the highest position where there is a smaller portion of material (vertically) above. When the material starts to deform, shear stresses increase gradually their importance in the role of breaking down the material. The shape evolution from a starting trapezoidal form generally ends with a configuration where occurs an accumulation

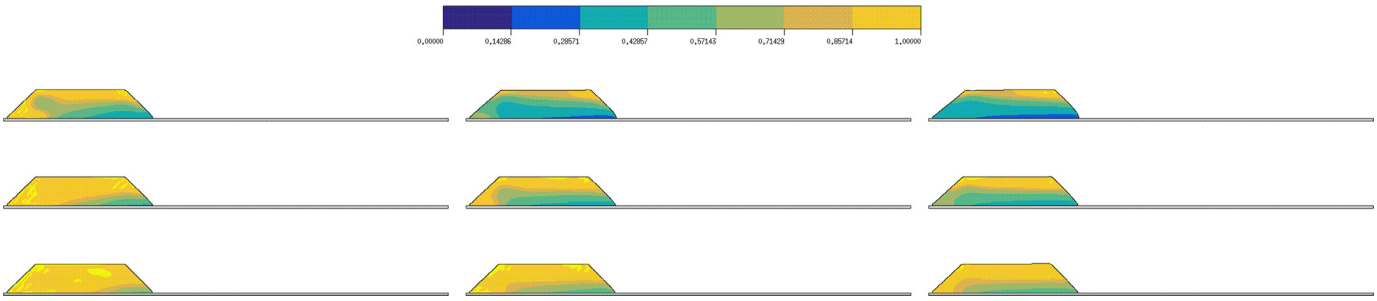

Fig. 4. Numerical prediction of the structure parameter λ at the dimensionless time $t = 25$ using $Wi = 0.1$, $K = 0.5$ and $t_{eq} = 100$. From (column) left to right: $\theta = 15^{\circ}, 30^{\circ}, 45^{\circ}$, and from (row) the top to bottom: $\tau_y = 0.2, 0.3, 0.4$.

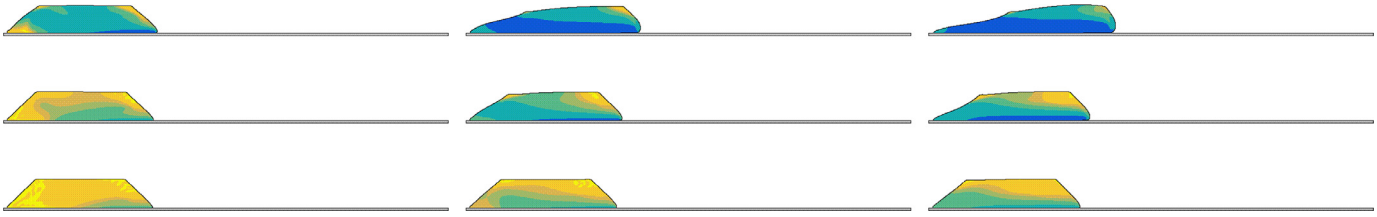

Fig. 5. Numerical prediction of the structure parameter λ at the dimensionless time $t = 50$ using $Wi = 0.1$, $K = 0.5$ and $t_{eq} = 100$. From (column) left to right: $\theta = 15^{\circ}, 30^{\circ}, 45^{\circ}$, and from (row) the top to bottom: $\tau_y = 0.2, 0.3, 0.4$.

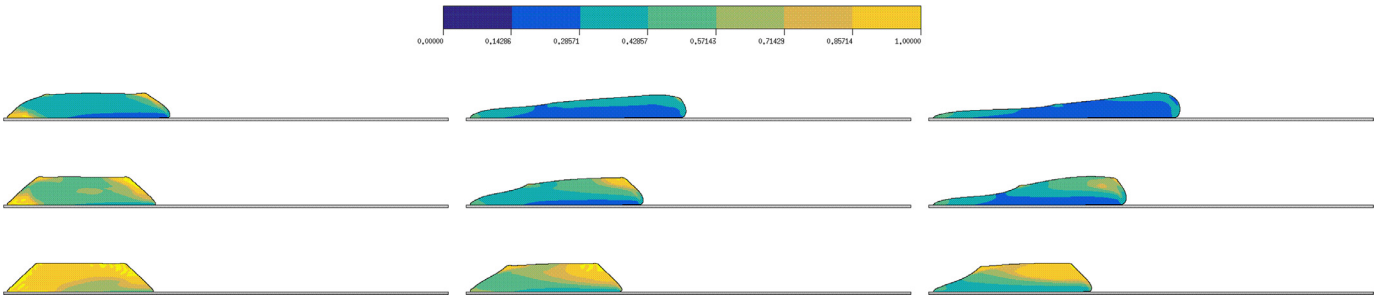

Fig. 6. Numerical prediction of the structure parameter λ at the dimensionless time $t = 75$ using $Wi = 0.1$, $K = 0.5$ and $t_{eq} = 100$. From (column) left to right: $\theta = 15^{\circ}, 30^{\circ}, 45^{\circ}$, and from (row) the top to bottom: $\tau_y = 0.2, 0.3, 0.4$.

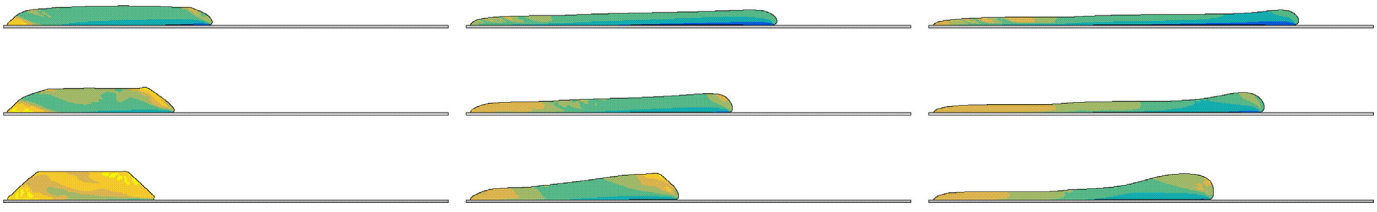

Fig. 7. Numerical prediction of the structure parameter λ at the dimensionless time $t = 200$ using $Wi = 0.1$, $K = 0.5$ and $t_{eq} = 100$. From (column) left to right: $\theta = 15^{\circ}, 30^{\circ}, 45^{\circ}$, and from (row) the top to bottom: $\tau_y = 0.2, 0.3, 0.4$.

of material in the moving front forming a kind of "head" while a "tail" is formed behind. At time $tU_c/L_c = 50$, Fig. 5, we notice that cases ($\theta = 45^{\circ}$, $\tau_y = 0.2$) and ($\theta = 30^{\circ}$, $\tau_y = 0.2$) had already departed from trapezoidal shape and are significantly broken in the parts near the solid surface. We notice that in the tail breaking occurs at high rates, even without having much material above. This happens because the no-slip condition induces high deformation rates and consequently high stresses in this region. The part of the material that is more "protected" from rejuvenation is the one located at the upper front corner of the trapezoid, since gravity effects and shear stresses are weaker in this region. After that, and until the last time shown ($tU_c/L_c = 200$) the evolution is such that higher angles induce less uniform evolutions in the sense that the head becomes much thicker than the tail. The intense destruction of the materials with lower yield stresses that happens at the early stages of the problem induces the formation of thin shapes very rapidly. This configuration is less susceptible to high gravity and shear stresses. In this scenario, a build-up process takes place, specially at the tail and at the upper front corner, as illustrated in Fig. 7 corresponding to $tU_c/L_c = 200$. It seems that the aging process is responsible for the passage from the accelerating regime to the retardation one.

In Fig. 8, we have investigated the influence of the Weissenberg number together with inclination. There is no significant change between $Wi = 0.01$ and $Wi = 0.1$, what is probably an indication that elasticity is not important at these levels. However, when $Wi = 1$ we can notice a more pronounced effect on the distance achieved by the material. This high Weissenberg number leads to a longer distance covered by the material, when the inclination angle is fixed.

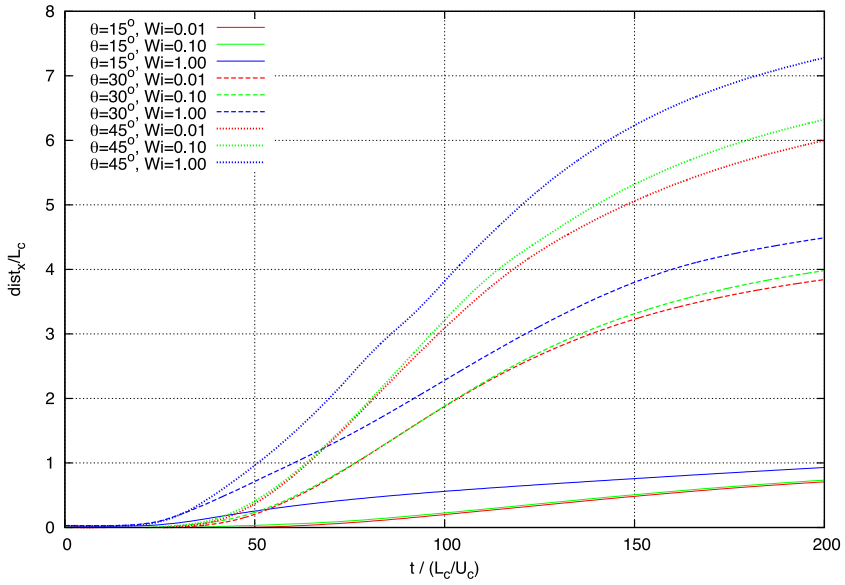

Fig. 8. Time variation of the front position, $dist_x$, varying the inclination angle and the Weissenberg number.

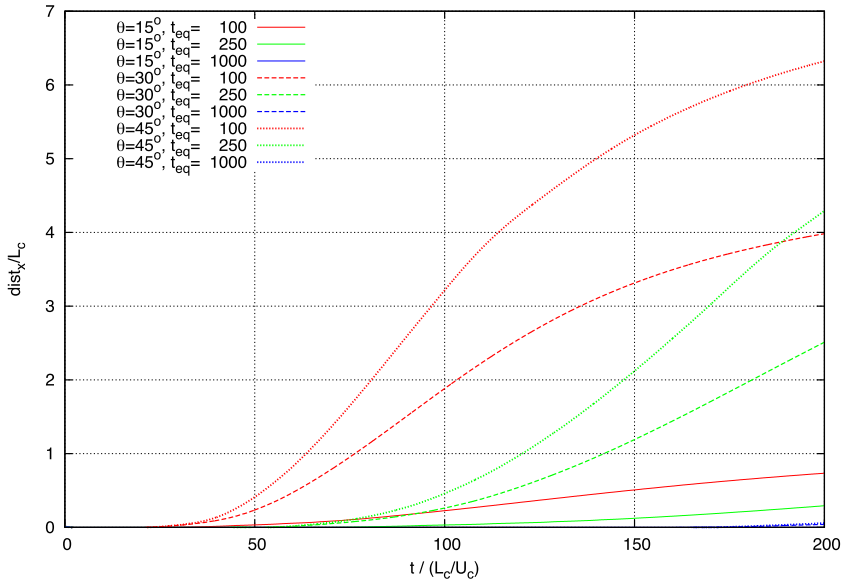

Fig. 9. Time variation of the front position, $dist_x$, varying the inclination angle and the thixotropic equilibrium time.

Fig. 9 shows how $dist_x$ evolves over time exploring the thixotropic dimensionless number, t_{eq}, together with inclination. The other conditions are fixed at $Wi = 0.1$, $K = 0.5$, and $\tau_y = 0.3$. As expected, increasing t_{eq} leads to a slower advance of the front of the material, since higher values of t_{eq} represents a longer time to adjust microstructure with respect to the new stress state. Interestingly, the range associated with the accelerating regime increased substantially when t_{eq} was raised from $t_{eq} = 100$ to $t_{eq} = 250$. The curves associated with $t_{eq} = 1000$ show that there were almost no progress along the inclined plane. The discrepancies associated with inclination angles obeyed the same trend analyzed previously, i.e. higher inclinations lead to higher rejuvenation rates.

Figs. 10 and 11 illustrate how shape and structure parameter are affected by the thixotropic time for the fixed inclination angle of $\theta = 30^\circ$ and the rest of the parameters as in Fig. 9. We can see by the comparing the columns of these figures that the breaking down rate of the material is clearly postponed in the case higher t_{eq} values, as expected. The evolution of each t_{eq} value is similar if we discount an appropriate elapsing time. Here we can notice that for the $t_{eq} = 1000$ case there was almost no change in shape until $tU_c/L_c = 200$, but we can notice that the structure parameter kept changing during this process.

As discussed previously, the three ranges that are generally present in the flow curve of a viscoplastic material are not captured by the Bingham or the Hershel–Bulkley models. In this connection, we investigate how the presence of the power-law range changes the results provided by the Bingham model (where $K = 0$).

Fig. 12 shows the dimensionless longitudinal distance covered by the material during the firsts 200 units of dimensionless time, tU_c/L_c for a number of cases where the inclination angle, the Weissenberg number, and the dimensionless thixotropic time are maintained fixed at values: $\theta = 30^\circ$, $Wi = 0.01$, and $t_{eq} = 100$, respectively. It is worth noticing that the values of K and plastic number τ_y and the dimensionless viscosity, η_∞ are complementaries with respect to unity. For fixed values of K, the results are quite intuitive. Increasing the plastic number, it becomes harder to break

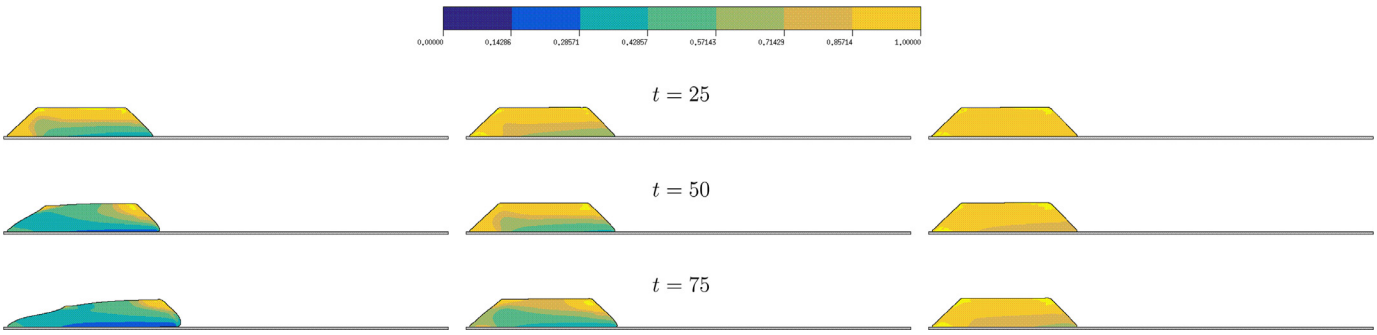

Fig. 10. Numerical prediction of the structure parameter λ using $\theta = 30^{\circ}$, $K = 0.5$, $\tau_y = 0.3$ and $Wi = 0.1$. From (column) left to right: $t_{eq} = 100$, $t_{eq} = 250$, $t_{eq} = 1000$.

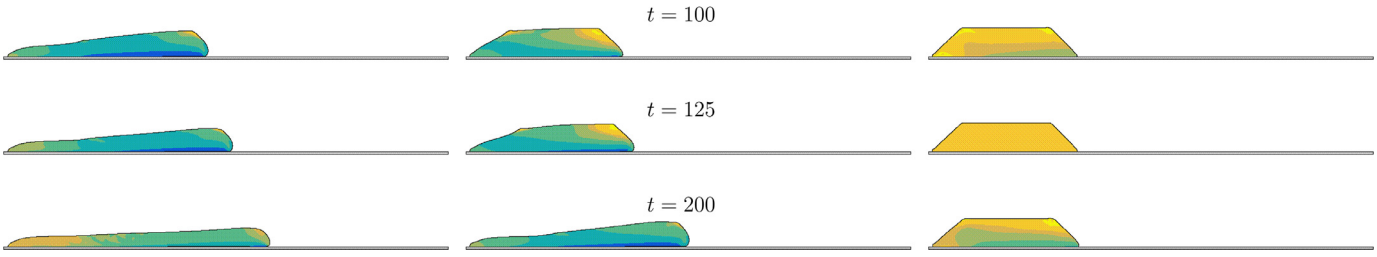

Fig. 11. Continuing. Numerical prediction of the structure parameter λ using $\theta = 30^{\circ}$, $K = 0.5$, $\tau_y = 0.3$ and $Wi = 0.1$. From (column) left to right: $t_{eq} = 100$, $t_{eq} = 250$, $t_{eq} = 1000$.

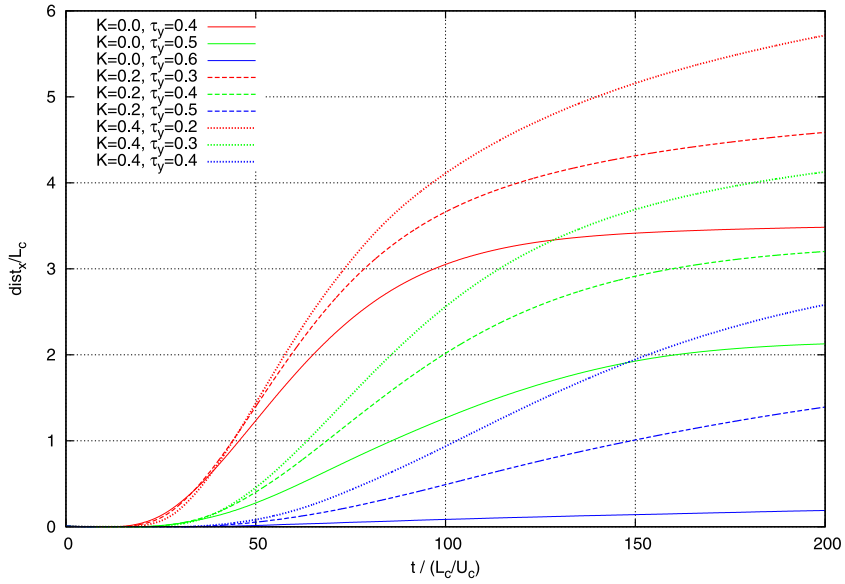

Fig. 12. Time variation of the front position, $dist_x$, varying the consistency index and the plastic number and fixing $Wi = 0.01$.

down the material and, therefore, it takes a longer period of time to achieve the same distance. From a comparison between the curves $(K = 0, \tau_y = 0.4)$ and $(K = 0.2, \tau_y = 0.4)$, where the plastic number is the same, we notice that the difference between the covered distances reached by these materials increases during a first stage, but at a certain instant, corresponding to $tU_c/L_c \approx 200$, this difference starts to decrease becoming small at $tU_c/L_c = 200$. This happens because during the firsts steps of the process, the stress intensity induced by gravity is able to impose a higher shear rate to the material corresponding to $(K = 0, \tau_y = 0.4)$, since the constant viscosity range is achieved for a larger portion of the domain. The same trend is found for the case where K is raised once more, $(K = 0.4, \tau_y = 0.4)$, namely the distance difference increases at a first stage and then decreases with respect to the $(K = 0, \tau_y = 0.4)$ case. Although this difference remains quite constant with respect to the $(K = 0.2, \tau_y = 0.4)$ case, it seems that it will decrease for future times. The curves corresponding to the cases $(K = 0, \tau_y = 0.6)$, $(K = 0.2, \tau_y = 0.4)$, and $(K = 0.4, \tau_y = 0.2)$ have the same η_∞. We can notice how spread are the results, what in turn means that the variables K and τ_y affect the transient motion in the inclined plane more significantly.

The progress of $dist_x$ in time of this set of cases is shown in Fig. 13. In general, we can observer a shorter accelerating regime more pronounced for the $K = 0$ cases. However, we found larger values for $dist_x$ at the final time $tU_c/L_c = 200$. The same sets of three curves are observed, i.e. in the accelerating regime, red, green, and blue curves evolve separately from each other.

Again, after showing the dimensionless distance $dist_x$ we show the materials evolve in deformation together with the field of structure parameter. This sequence is shown from Figs. 14–19. The

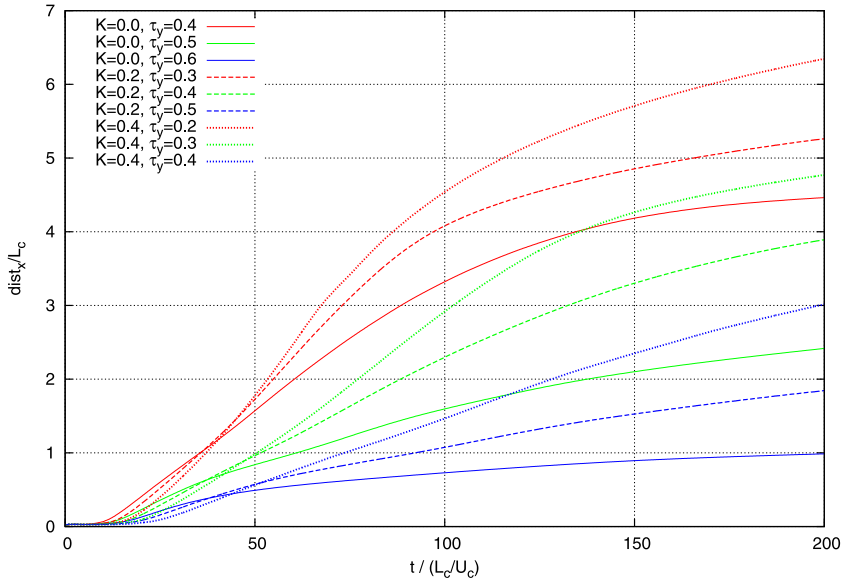

Fig. 13. Time variation of the front position, $dist_x$, varying the consistency index and the plastic number and fixing $Wi = 1$. (For interpretation of the references to color in the text, the reader is referred to the web version of this article.)

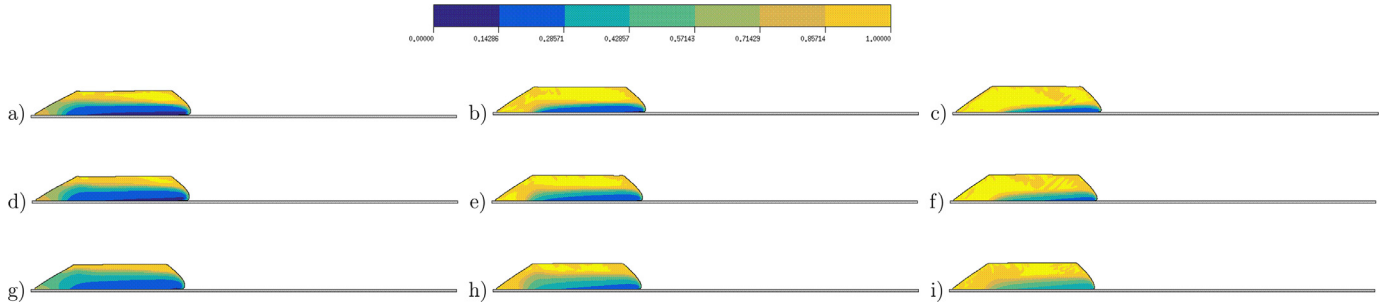

Fig. 14. Numerical prediction of the structure parameter λ at the dimensionless time $t = 25$ using $Wi = 1$, $\theta = 30^\circ$ and $t_{eq} = 100$: a) $K = 0.0$ and $\tau_y = 0.4$, b) $K = 0.0$ and $\tau_y = 0.5$, c) $K = 0.0$ and $\tau_y = 0.6$, d) $K = 0.2$ and $\tau_y = 0.3$, e) $K = 0.2$ and $\tau_y = 0.4$, f) $K = 0.2$ and $\tau_y = 0.5$, g) $K = 0.4$ and $\tau_y = 0.2$, h) $K = 0.4$ and $\tau_y = 0.3$, i) $K = 0.4$ and $\tau_y = 0.4$.

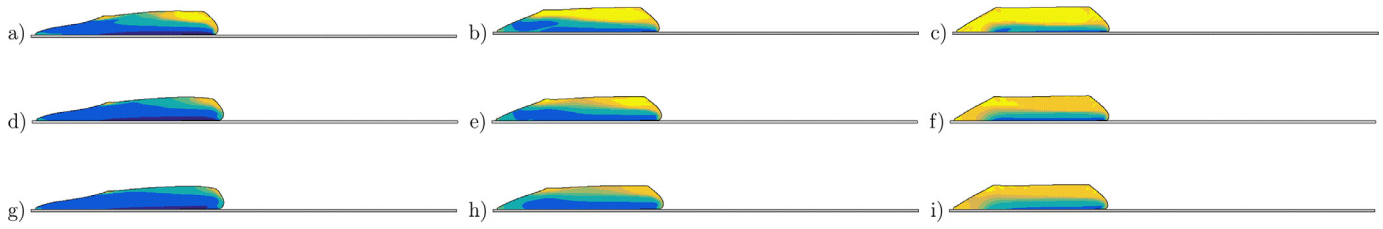

Fig. 15. Numerical prediction of the structure parameter λ at the dimensionless time $t = 50$ using $Wi = 1$, $\theta = 30^\circ$ and $t_{eq} = 100$: a) $K = 0.0$ and $\tau_y = 0.4$, b) $K = 0.0$ and $\tau_y = 0.5$, c) $K = 0.0$ and $\tau_y = 0.6$, d) $K = 0.2$ and $\tau_y = 0.3$, e) $K = 0.2$ and $\tau_y = 0.4$, f) $K = 0.2$ and $\tau_y = 0.5$, g) $K = 0.4$ and $\tau_y = 0.2$, h) $K = 0.4$ and $\tau_y = 0.3$, i) $K = 0.4$ and $\tau_y = 0.4$.

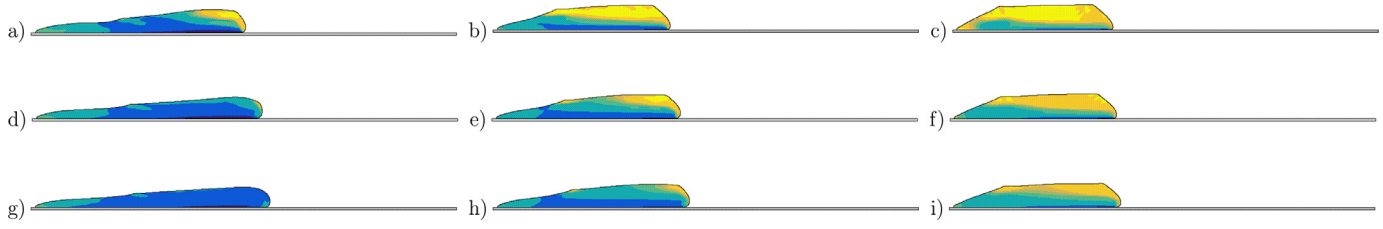

Fig. 16. Numerical prediction of the structure parameter λ at the dimensionless time $t = 75$ using $Wi = 1$, $\theta = 30^\circ$ and $t_{eq} = 100$: a) $K = 0.0$ and $\tau_y = 0.4$, b) $K = 0.0$ and $\tau_y = 0.5$, c) $K = 0.0$ and $\tau_y = 0.6$, d) $K = 0.2$ and $\tau_y = 0.3$, e) $K = 0.2$ and $\tau_y = 0.4$, f) $K = 0.2$ and $\tau_y = 0.5$, g) $K = 0.4$ and $\tau_y = 0.2$, h) $K = 0.4$ and $\tau_y = 0.3$, i) $K = 0.4$ and $\tau_y = 0.4$.

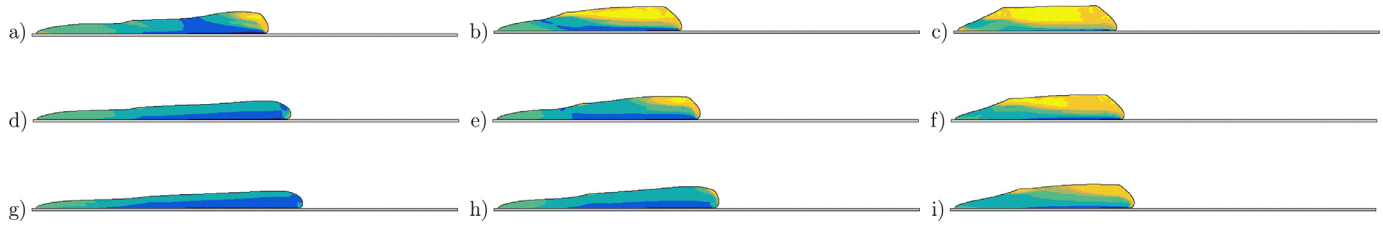

Fig. 17. Numerical prediction of the structure parameter λ at the dimensionless time $t = 100$ using $Wi = 1$, $\theta = 30^{\circ}$ and $t_{eq} = 100$: a) $K = 0.0$ and $\tau_y = 0.4$, b) $K = 0.0$ and $\tau_y = 0.5$, c) $K = 0.0$ and $\tau_y = 0.6$, d) $K = 0.2$ and $\tau_y = 0.3$, e) $K = 0.2$ and $\tau_y = 0.4$, f) $K = 0.2$ and $\tau_y = 0.5$, g) $K = 0.4$ and $\tau_y = 0.2$, h) $K = 0.4$ and $\tau_y = 0.3$, i) $K = 0.4$ and $\tau_y = 0.4$.

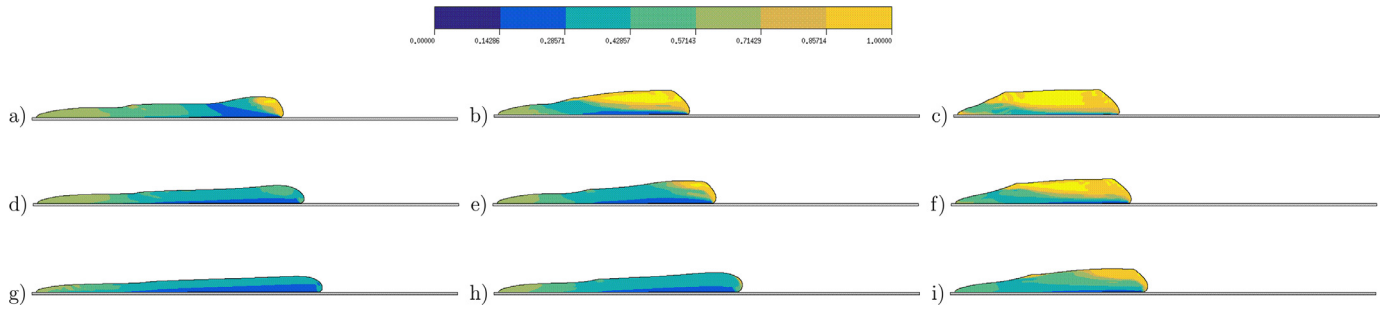

Fig. 18. Numerical prediction of the structure parameter λ at the dimensionless time $t = 125$ using $Wi = 1$, $\theta = 30^{\circ}$ and $t_{eq} = 100$: a) $K = 0.0$ and $\tau_y = 0.4$, b) $K = 0.0$ and $\tau_y = 0.5$, c) $K = 0.0$ and $\tau_y = 0.6$, d) $K = 0.2$ and $\tau_y = 0.3$, e) $K = 0.2$ and $\tau_y = 0.4$, f) $K = 0.2$ and $\tau_y = 0.5$, g) $K = 0.4$ and $\tau_y = 0.2$, h) $K = 0.4$ and $\tau_y = 0.3$, i) $K = 0.4$ and $\tau_y = 0.4$.

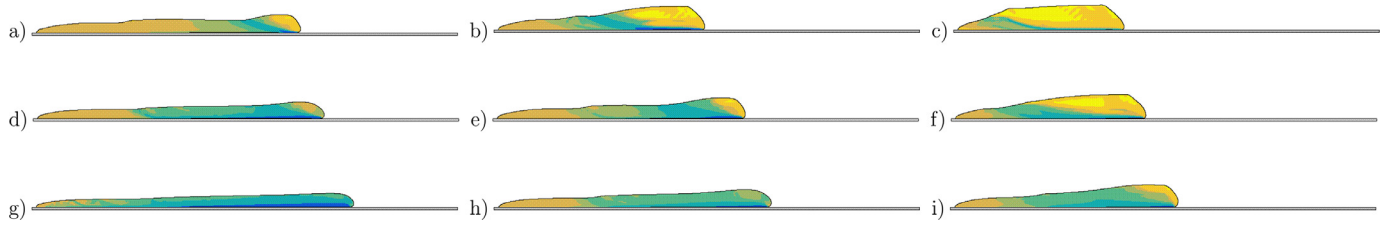

Fig. 19. Numerical prediction of the structure parameter λ at the dimensionless time $t = 200$ using $Wi = 1$, $\theta = 30^{\circ}$ and $t_{eq} = 100$: a) $K = 0.0$ and $\tau_y = 0.4$, b) $K = 0.0$ and $\tau_y = 0.5$, c) $K = 0.0$ and $\tau_y = 0.6$, d) $K = 0.2$ and $\tau_y = 0.3$, e) $K = 0.2$ and $\tau_y = 0.4$, f) $K = 0.2$ and $\tau_y = 0.5$, g) $K = 0.4$ and $\tau_y = 0.2$, h) $K = 0.4$ and $\tau_y = 0.3$, i) $K = 0.4$ and $\tau_y = 0.4$.

first feature of the distribution of structure parameter that calls the attention is the fact that at the early stages, there is a sharper change between fully structure (dark red) and mostly unstructured (blue) regions. There are almost no intermediate regions and the more structured state occupies a larger portion of the domain. The relative increase in elasticity has diminish the importance of shear stress and what we see at $tU_c/L_c = 25$, Fig. 14, is associated with the stress that equilibrates gravitational forces. The remaining part of the domain experiences a strong breakdown process, more pronounced for lower values of K and τ_y, i.e. when η_∞ is high (column corresponding to the cases a)-d)-g)). The evolution occurs with less destruction in the original unyielded regions when compared with the less elastic counterpart. It seems that the less viscous layer near the inclined plane acts as a lubricating material and induces higher deformations. A build up process takes place specially at the tail and also in the middle in the cases where the material assumes an elongated configuration as it can be seen in Figs. 17–19.

When K is increased and the material has a more important power-law range in the flow curve, the scenarios become more complex. In Fig. 20, the colors are associated with fixed values of η_∞. We can notice that keeping K fixed, the behavior of $dist_x$ can be rather different, depending on the plastic number. The same happens for fixed η_∞ (same colors). When the plastic number is fixed the material tends to exhibit a more similar behavior than fixing other quantities, as exemplified by the curves with $\tau_y = 0.3$. In these cases, increasing K decreases the value of $dist_x$. Again, higher values of η_∞ leads to a higher portion of the material having the lowest structure level as an attractor for the current state, what induces higher rejuvenation.

When the overall elasticity is raised from $Wi = 0.01$ to $Wi = 1$, the curves do not change their relative positions, as shown in Fig. 21. However, we can notice that a higher value of $dist_x$ is achieved when Wi is higher, as already reported.

The combined variation of plastic number and Weissenberg number, as illustrated in Fig. 22, shows that changing τ_y in this range is more significant than changing Weissenberg number. Although we can see that at least from $Wi = 0.1$ to $Wi = 1$, elastic effects have an influence on the distance covered by the material, plastic number clearly splits the general cases into the groups of constant values of this parameter. In the case of Fig. 22 increasing plastic number is to decrease the viscosity contribution, η_∞, since K is fixed.

Because of the transient nature of the problem analyzed, we have produced some movies that are available as a supplementary material (see Electronic Annex 1 in the online version of this submitted paper). These movies are related to Figs. 4–9 (secondary diagonal) and two additional ones have been created to highlight the influence of the plastic number and the thixotropic equilibrium time during the transient process of the "avalanche effect". As in the figures of the present manuscript, the movies show the evolution of the structure parameter and of the shape and posi-

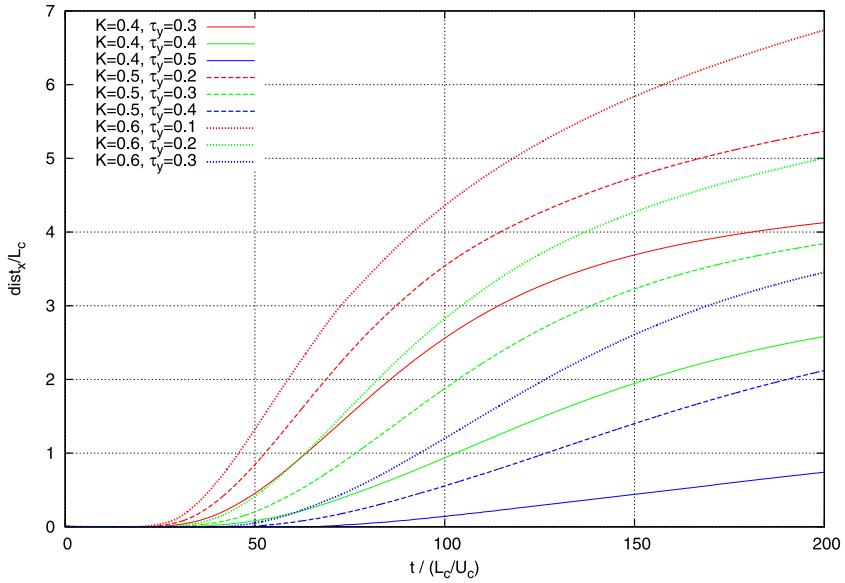

Fig. 20. Time variation of the front position, $dist_x$, varying the consistency index and the plastic number and fixing $Wi = 0.01$. (For interpretation of the references to color in the text, the reader is referred to the web version of this article.)

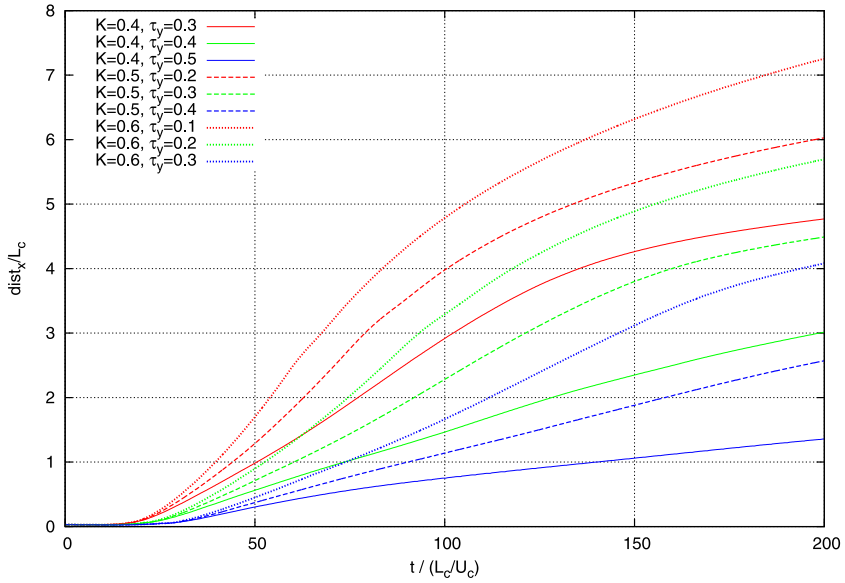

Fig. 21. Time variation of the front position, $dist_x$, varying the consistency index and the plastic number and fixing $Wi = 1$.

tion of the material with respect to the inclined plane, helping to improve the visualization and the understanding of the present problem.

5. Concluding remarks

In the present work we analyzed the free-surface problem of an elasto-viscoplastic thixotropic material on an inclined plane subjected to the gravity force. The initial state of the material is fully structured and its motion occurs as a consequence of the breaking down process in the regions where the stresses induced by gravity overcome the yield stress of the material.

This investigation was conducted by using a finite difference formulation recently proposed in [28]. In summary, the incompressible unsteady Navier–Stokes equations were solved via projection method applying the Crank–Nicolson/Adam–Bashforth scheme to time-discretize the momentum equation while the constitutive equation for the non-Newtonian tensor was treated by the second order Runge–Kutta method. Based in a combined MAC and front-tracking approach, an implicit discretization was applied in the free-surface normal stress condition resulting in a stable formulation for solving moving interface problems. In order to take into account the thixotropic behavior of the material, a conventional iterative scheme was employed for solving an extended Herschel–Bulkley model equation while the transport equation for the structure parameter was computed by a semi-implicit scheme.

The constitutive model employed has an embedded equation for the flow curve that contains three dimensionless parameters that encompasses the advantage of the Bingham model, the prediction of non-vanishing viscosity for high shear rates, together with the advantage of the Herschel–Bulkley model, an asymptotic approach to the yield stress in the limit of small values of shear rate. Choosing the maximum stress of the domain as the characteristic stress the dimensionless parameters that compose the flow curve are restricted to $\tau_y^* + K^* + \eta_\infty^* = 1$. The other important pa-

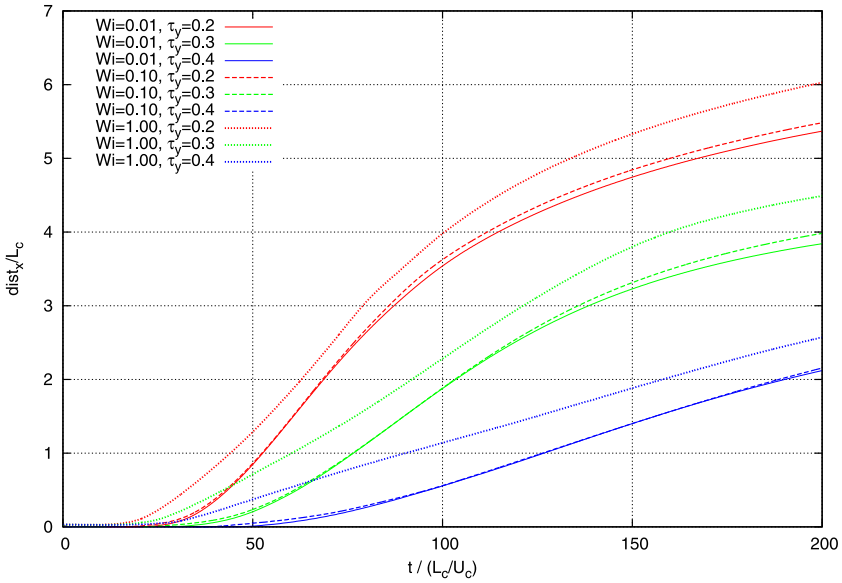

Fig. 22. Time variation of the front position, $dist_x$, varying the plastic number and Weissenberg number.

rameters analyzed are: the dimensionless thixotropic time, t_{eq}, the Weissenberg number, *Wi*, and the inclination angle, θ.

The so-called *avalanche effect*, i.e. the self-reinforcing process where the rejuvenation process induces motion what in turn induces additional rejuvenation was found to happen in every case, at least at a first stage of the evolution of the material. This process can be detected by the acceleration of the front of the material. The results obtained in the range investigated indicate that high values of the plastic number, low inclination angles, high elastic effects, and high values of t_{eq} favor the accelerating regime, which can eventually happen throughout the whole domain. On the other hand, the opposite qualitative tendency of the dimensionless parameters can lead to a thin layer of material after a relatively low elapsed time. This configuration is no longer significantly affected by the stresses induced by gravity and a build up process is initiated. During this period, the material starts a retardation process a sign that the material will stop.

Generally speaking, the most determinant property associated with the evolution of the material over the inclined plane is the yield stress, evaluated by the plastic number, in the intuitive direction, i.e. increasing τ_y^* makes the material harder to break down. However, the combination of K^* and η_∞^* can lead to rather different evolutions showing that the both parameters that detach the material from the more classical Bingham and Herschel–Bulkley viscoplastic models play an important role in the process. For fixed values of the plastic number higher η_∞^* induces more breakage, since this parameter is associated with the lowest structuring level of the material and a large η_∞^* increases the driving stress potential for rejuvenation.

The results concerning changes in elastic effects as represented by the Weissenberg number were less intuitive. In this connection, the evolution of the configuration of the material, together with the structure parameter were helpful on understanding the overall process. Increasing elasticity, induces a higher deformation with no breaking, hence a more abrupt change of structure state from the fully structured one to a low structuring level state takes place in the domain. Therefore the shear rate near the inclined plane increases, what in turn induces the material to progress more rapidly on the inclined plane.

Changes on inclination angle and thixotropic time lead to intuitive responses. Increasing inclination induces higher rejuvenation rate and consequently a more rapid advancing front. Higher values of thixotropic time lead to slower changes in the structure parameter and the opposite trend happens.

The present approach was able to handle this important free-surface problem which is transient, and involves a complex material. An important feature of this problem is the fact that motion is a consequence of the stress distribution in the material, i.e. there is no imposed flow rate or initial velocity profile.

Acknowledgments

C.M. Oishi acknowledges the financial support of FAPESP (Fundação de Amparo à Pesquisa do Estado de São Paulo) Grant 2013/07375-0 and CNPq (Conselho Nacional de Desenvolvimento Cientifico e Tecnologico), Grant 307459/2016-0. R.L. Thompson acknowledges CNPq (Conselho Nacional de Desenvolvimento Cientifico e Tecnologico), Grant 309004/2014-4.

Supplementary material

Supplementary material associated with this article can be found, in the online version, at 10.1016/j.jnnfm.2017.07.001.

References

[1] H.A. Barnes, Thixotropy—a review, J. Non-Newtonian Fluid Mech. 70 (1997) 1–33.
[2] A. Mujumdar, A.N. Beris, A.B. Metzner, Transient phenomena in thixotropic systems, J. Non-Newtonian Fluid Mech. 102 (2002) 157–178.
[3] J. Mewis, N.J. Wagner, Thixotropy, Adv. Colloid Interface Sci. 147–148 (2009) 214–227.
[4] P.R. de Souza Mendes, R.L. Thompson, A critical overview of elasto-viscoplastic thixotropic modeling, J. Non-Newtonian Fluid Mech. 187–188 (2012) 8–15.
[5] N.J. Balmforth, I.A. Frigaard, G. Ovarlez, Yielding to stress: recent developments in viscoplastic fluid mechanics, Ann. Rev. Fluid Mech. 46 (2014) 121–146.
[6] P. Coussot, Yield stress fluid flows: a review of experimental data, J. Non-Newtonian Fluid Mech. 211 (2014) 31–49.
[7] F. Yziquel, P.J. Carreau, M. Moan, P.A. Tanguy, Rheological modeling of concentrated colloidal suspensions, J. Non-Newtonian Fluid Mech. 86 (1999) 133–155.
[8] D. Quemada, Rheological modelling of complex fluids: IV: thixotropic and "thixoelastic" behaviour. start-up and stress relaxation, creep tests and hysteresis cycles, Eur. Phys. J. AP 5 (2) (1999) 191–208.
[9] F. Bautista, J.M. de Santos, J.E. Puig, O. Manero, Understanding thixotropic and antithixotropic behavior of viscoelastic micellar solutions and liquid crystalline dispersions. i. the model, J. Non-Newtonian Fluid Mech. 80 (1999) 93–113.
[10] K. Dullaert, J. Mewis, A structural kinetics model for thixotropy, J. Non-Newtonian Fluid Mech. 139 (2006) 21–30.
[11] P.R. de Souza Mendes, Modeling the thixotropic behavior of structured fluids, J. Non-Newtonian Fluid Mech. 164 (2009) 66–75.

[12] C.J. Dimitriou, G.H. McKinley, A comprehensive constitutive law for waxy crude oil: a thixotropic yield stress fluid, Soft Matter 10 (35) (2014) 6619–6644.
[13] J.E. López-Aguilar, M.F. Webster, H. Tamaddon-Jahromi, O. Manero, Numerical modelling of thixotropic and viscoelastoplastic materials in complex flows, Rheol. Acta 54 (2015) 307–325.
[14] N. Dubash, N.J. Balmforth, A.C. Slima, S. Cochard, What is the final shape of a viscoplastic slump? J. Non-Newtonian Fluid Mech. 158 (2009) 91–100.
[15] L. Staron, P.Y. Lagrée, P. Ray, S. Popinet, Scaling laws for the slumping of a bingham plastic fluid, J. Rheol. (57) (2013) 1265–1280.
[16] N. Pashias, D.V. Boger, J. Summers, D.J. Glenister, A fifty cent rheometer for yield stress measurement, J. Rheol. 40 (1996) 1179–1189.
[17] N. Roussel, P. Coussot, "Fifty-cent rheometer" for yield stress measurements: from slump to spreading flow, J. Rheol. 49 (2005) 705–718.
[18] N.J. Balmforth, R.V. Craster, P. Perona, A.C. Rust, R. Sassi, Viscoplastic dam breaks and the bostwick consistometer, J. Non-Newtonian Fluid Mech. 142 (2007) 63–78.
[19] C. Ancey, S. Cochard, The dam-break problem for Herschel-Bulkley viscoplastic fluids down steep flumes, J. Non-Newtonian Fluid Mech. 158 (2009) 18–35.
[20] Y. Liu, N.J. Balmforth, S. Hormozi, D.R. Hewitt, Two-dimensional viscoplastic dambreaks, J. Non-Newtonian Fluid Mech. 238 (2016) 65–79.
[21] D.R. Hewitt, N.J. Balmforth, Thixotropic gravity currents, J. Fluid Mech. 727 (2013) 56–82.
[22] P. Coussot, Q.D. Nguyen, H.T. Huynh, D. Bonn, Viscosity bifurcation in thixotropic, yielding fluids, J. Rheol. 46 (2002a) 573–589.
[23] P. Coussot, Q.D. Nguyen, H.T. Huynh, D. Bonn, Avalanche behavior in yield stress fluids, Phys. Rev. Letters 88 (175501) (2002b) 1–4.
[24] P.R. de Souza Mendes, Thixotropic elasto-viscoplastic model for structured fluids, Soft Matter 7 (2011) 2471–2483.
[25] P.R. de Souza Mendes, R.L. Thompson, A unified approach to model elasto-viscoplastic thixotropic yield-stress materials and apparent yield-stress fluids, Rheol. Acta 52 (2013) 673–694.
[26] P.R. de Souza Mendes, K.R. Rajagopal, R.L. Thompson, A thermodinamic framework to model thixotropic materials, Int. J. Non-Linear Mech. 55 (2013) 48–54.
[27] S. Frey, F.B. Link, R.L. Thompson, M.F. Naccache, P.R. de Souza Mendes, Plane flow of thixotropic elasto-viscoplastic materials through a 1:4 sudden expansion, J. Non-Newtonian Fluid Mech. 220 (2015) 162–174.
[28] C.M. Oishi, R.L. Thompson, F.P. Martins, Transient motions of elasto-viscoplastic thixotropic materials subjected to an imposed stress field and to stress-based free-surface boundary conditions, Int. J. Eng. Sci. 109 (2016) 165–201.
[29] R.L. Thompson, E.J. Soares, Viscoplastic dimensionless numbers, J. Non-Newtonian Fluid Mech. 238 (2016) 57–64.
[30] C.M. Oishi, F.P. Martins, M.F. Tomé, J.A. Cuminato, S. McKee, Numerical solution of the extended pom-pom model for viscoelastic free surface flows, J. Non-Newtonian Fluid Mech. 166 (2011) 165–179.
[31] J.A. Cuminato, C.M. Oishi, R.A. Figueiredo, et al., Implicit methods for simulating low Reynolds number free surface flows: Improvements on the MAC-type methods, in: M. Wakayama, et al. (Eds.), The Impact of Applications on Mathematics, Springer Japan, 2014.